Monthly Notices
of the
ROYAL ASTRONOMICAL SOCIETY

Mon. Not. R. Astron. Soc. **407,** 1933–1945 (2010) doi:10.1111/j.1365-2966.2010.17039.x

Modelling shear flows with smoothed particle hydrodynamics and grid-based methods

Veronika Junk,[1⋆] Stefanie Walch,[2] Fabian Heitsch,[3] Andreas Burkert,[1] Markus Wetzstein,[4] Marc Schartmann[1,5] and Daniel Price[6]

[1] *University Observatory Munich, Scheinerstrasse 1, 81679 Munich, Germany*
[2] *School of Physics and Astronomy, Cardiff University, The Parade, Roath, Cardiff CF24 3AA*
[3] *Department of Astronomy, University of Michigan, 500 Church St, Ann Arbor, MI 48109-1042, USA*
[4] *Department of Astrophysical Sciences, Princeton University, Princeton, NJ 08544, USA*
[5] *Max Planck Institute for Extraterrestrial Physics, Giessenbachstrasse, 85748 Garching, Germany*
[6] *School of Mathematical Sciences, Monash University, Clayton, VIC 3168, Australia*

Accepted 2010 May 18. Received 2010 May 18; in original form 2009 August 16

ABSTRACT

Given the importance of shear flows for astrophysical gas dynamics, we study the evolution of the Kelvin–Helmholtz instability (KHI) analytically and numerically. We derive the dispersion relation for the two-dimensional KHI including viscous dissipation. The resulting expression for the growth rate is then used to estimate the intrinsic viscosity of four numerical schemes depending on code-specific as well as on physical parameters. Our set of numerical schemes includes the Tree-SPH code VINE, an alternative smoothed particle hydrodynamics (SPH) formulation developed by Price and the finite-volume grid codes FLASH and PLUTO. In the first part, we explicitly demonstrate the effect of dissipation-inhibiting mechanisms such as the Balsara viscosity on the evolution of the KHI. With VINE, increasing density contrasts lead to a continuously increasing suppression of the KHI (with complete suppression from a contrast of 6:1 or higher). The alternative SPH formulation including an artificial thermal conductivity reproduces the analytically expected growth rates up to a density contrast of 10:1. The second part addresses the shear flow evolution with FLASH and PLUTO. Both codes result in a consistent non-viscous evolution (in the equal as well as in the different density case) in agreement with the analytical prediction. The viscous evolution studied with FLASH shows minor deviations from the analytical prediction.

Key words: hydrodynamics – instabilities – methods: analytical – methods: numerical – ISM: kinematics and dynamics.

1 INTRODUCTION

Shear flows are an integral part of many astrophysical processes, from jets, the formation of cold streams, to outflows of protostars (Diemand et al. 2008; Agertz, Teyssier & Moore 2009; Dekel et al. 2009; Walch et al. 2010), and cold gas clouds falling through the diffuse hot gas in dark matter haloes (Bland-Hawthorn et al. 2007; Burkert et al. 2008). Jets and outflows of young stars can entrain ambient material, leading to mixing and possibly the generation of turbulence in e.g. molecular clouds (Burkert 2006; Banerjee, Klessen & Fendt 2007; Carroll et al. 2009; Gritschneder et al. 2009b), while the dynamical interaction of cold gas clouds with the background galactic halo medium can lead to gas stripping of e.g. dwarf spheroidals (e.g. Grcevich, Heitsch & Putman 2010), and the disruption of high-velocity clouds (Quilis & Moore 2001; Heitsch & Putman 2009). The Kelvin–Helmholtz instability (KHI) is believed to significantly influence the gas dynamics in all of these different scenarios.

Moreover, viscous flows play a crucial role in e.g. gas accretion on to galactic discs (Das & Chattopadhyay 2008; Heinzeller, Duschl & Mineshige 2009; Park 2009), as well as in dissipative processes like the turbulent cascade. Typically, the gas viscosity seems to be rather low in the interstellar medium, with typical flow Reynolds numbers of 10^5.

To describe these complex processes in detail, numerical schemes are applied to follow the hydrodynamical evolution. Numerous simulations use smoothed particle hydrodynamics (SPH), (Gingold & Monaghan 1977; Lucy 1977; Benz 1990; Monaghan 1992, 2005), because its Lagrangian approach allows us to follow the evolution to high densities and small spatial scales. In combination with *N*-body codes, it is a perfect tool for cosmological simulations

⋆E-mail: vjunk@usm.uni-muenchen.de

(e.g. Hernquist & Katz 1989; Couchman, Thomas & Pearce 1995; Springel & Hernquist 2002; Marri & White 2003; Serna, Domínguez-Tenreiro & Sáiz 2003) and galaxy formation and evolution (Katz, Hernquist & Weinberg 1992; Evrard, Summers & Davis 1994; Navarro, Frenk & White 1995; Steinmetz & Navarro 1999; Thacker & Couchman 2000; Steinmetz & Navarro 2002; Naab, Jesseit & Burkert 2006). SPH describes the physical properties of a fluid by smoothing over a representative set of particles. However, this can lead to several problems. It can fail to correctly model sharp density gradients such as contact discontinuities, or velocity gradients occurring in e.g. shear flows (see Agertz et al. 2007), thus suppressing shear instabilities such as the KHI.

An interesting problem to test the limitations of SPH as well as grid codes is the passage of a cold dense gas cloud moving through a hot and less dense ambient medium (Murray et al. 1993; Vietri, Ferrara & Miniati 1997; Agertz et al. 2007). Such a configuration would be typical for gas clouds raining on to galactic protodiscs, for high-velocity clouds in the Milky Way and for cold H I clouds in the Galactic disc. Murray et al. (1993) demonstrated using a grid code that in the absence of thermal instabilities and/or gravity clouds moving through a diffuse gas should be disrupted by hydrodynamical shear flow instabilities within the time they need to travel through their own mass. Agertz et al. (2007) have shown that the KHI, and therefore the disintegration of such clouds is suppressed in SPH simulations. This problem, in particular the suppression of the KHI, has been subject to recent discussion in the literature. Several solutions have been proposed, e.g. Price (2008) discusses a mechanism which involves a special diffusion term (see also Wadsley, Veeravalli & Couchman 2008).

Furthermore, Read, Hayfield & Agertz (2010) identify two effects occurring in the SPH formalism, each one separately contributing to the instability suppression. The first problem is related to the leading order error in the momentum equation, which should decrease with increasing neighbour number. However, numerical instabilities prevent its decline. By introducing appropriate kernels, Read et al. (2010) showed that this problem can be cured. The second problem arises due to the entropy conservation. Entropy conservation inhibits particle mixing and leads to a pressure discontinuity. This can be avoided by using a temperature-weighted density following Ritchie & Thomas (2001) (see also Price 2008). Recently, Abel (2010) has shown to reduce the leading error problem by using a novel discretization of the pressure equation, which smoothes the force on the kernel scale and improves the stability.

Another characteristic of SPH is the implementation of an artificial viscosity (AV) term (Monaghan & Gingold 1983), which is necessary in order to treat shock phenomena and to prevent particle interpenetration. AV can produce an artificial viscous dissipation in a flow corresponding to a decrease of the Reynolds number and therefore a suppression of the KHI (Monaghan 2005). To confine this effect, a reduction of viscous dissipation was proposed by Balsara (1995) and improved by Colagrossi (2004). Thacker et al. (2000) studied different AV implementations in SPH and pointed out that the actual choice of the AV implementation is the primary factor in determining code performance. Recently, Cartwright & Stamatellos (2010) showed that the use of the Balsara switch is not beneficial in non-convergent shear flows. An extension of SPH which includes physical fluid viscosities was discussed by e.g. Flebbe et al. (1994), Takeda, Miyama & Sekiya (1994), Español & Revenga (2003), Sijacki & Springel (2006) and Lanzafame, Belvedere & Molteni (2006).

An alternative to conventional numerical schemes may arise from a new class of hybrid schemes based on unstructured grids and combining the strengths of SPH and grid codes (Springel 2010). Some of the problems listed above might be solved with this type of implementation.

In this paper we determine how accurate shear flows and the corresponding incompressible KHI are described in common numerical schemes. Therefore, in Section 2, we analytically derive the growth rates of the KHI including viscosity. In Section 3 we briefly describe the numerical schemes and outline how the simulations have been analysed. We then discuss our results. At first, we concentrate on the standard SPH implementation, which does not contain a physical viscosity but instead uses AV. However, as mentioned above, AV does influence the evolution of the flow. In Section 4, we discuss the ability of two numerical SPH schemes to model the incompressible KHI, namely the Tree-SPH method VINE (Wetzstein et al. 2009; Nelson, Wetzstein & Naab 2009), and the SPH code of Price (2008).

By comparing to the derived analytical solution, we assess the effects of AV in VINE and estimate the intrinsic physical viscosity caused by AV (4.1). We then study the development of the KHI for different density contrasts (4.2). We show that the instability is suppressed for density contrasts equal to or larger than 6:1. We also discuss the remedy suggested by (Price 2008, hereafter P08).

In Section 5, we then study the same problem with two grid codes, FLASH (Fryxell et al. 2000) and PLUTO (Mignone et al. 2007). As the intrinsic AV is negligible in these schemes, we study the non-viscous as well as the viscous evolution of the KHI for equal (5.1) as well as non-equal (5.2) density layers. We summarize our findings in Section 6.

2 KHI – ANALYTICAL DESCRIPTION

To derive the growth rate of the KHI in two dimensions including viscosity, we follow the analysis of Chandrasekhar (1961) (for a related analysis see also Funada & Joseph 2001 and Kaiser et al. 2005). The fluid system is assumed to be viscous and incompressible. We use Cartesian coordinates in x and y, with two fluids at densities ρ_1, ρ_2, and velocities U_1, U_2 moving anti-parallel along the x-axis, separated by an interface layer at $y = y_s$ (see Fig. 1). We neglect the effect of self-gravity. The hydrodynamical equations for such a system are then given by the continuity equation

$$\frac{\partial}{\partial t}\rho + \nabla \cdot (\rho \boldsymbol{v}) = 0, \tag{1}$$

and the momentum equation

$$\rho \cdot \left[\frac{\partial \boldsymbol{v}}{\partial t} + (\boldsymbol{v} \cdot \nabla)\,\boldsymbol{v}\right] = -\nabla p + \rho \nu \triangle \boldsymbol{v}, \tag{2}$$

with the flow density ρ, velocity $\boldsymbol{v}$, the thermal pressure p and the kinematic viscosity ν.

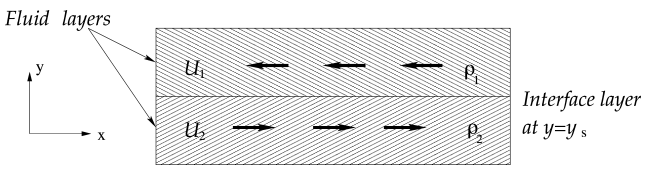

Figure 1. Sketch of the initial conditions considered. Two fluid layers with constant densities ρ_1 and ρ_2 flowing in opposite directions with uniform velocities U_1 and U_2.

2.1 Linear Perturbations

We linearize equations (1) and (2) with the perturbations

$$\boldsymbol{v} \rightarrow \boldsymbol{v} + \delta\boldsymbol{v} = [U(y) + u; w] \tag{3}$$

$$\rho \rightarrow \rho + \delta\rho, \tag{4}$$

$$p \rightarrow p + \delta p. \tag{5}$$

u, w express the perturbation in the velocity, $\delta\rho$ and δp in the density and pressure, respectively. This yields the system of linearized equations as

$$\rho\partial_t u + \rho U\partial_x u + \rho w\partial_y U = -\partial_x\delta p + \nu(\rho + \delta\rho)\partial_y^2 U + \rho\nu\left(\partial_x^2 + \partial_y^2\right)u, \tag{6}$$

$$\rho\partial_t w + \rho U\partial_x w = -\partial_y\delta p + \rho\nu\left(\partial_x^2 + \partial_y^2\right)w, \tag{7}$$

$$\partial_t\delta\rho + U\partial_x\delta\rho = -w\partial_y\rho, \tag{8}$$

$$\partial_t\delta y_s + U_s\partial_x\delta y_s = -w(y_s), \tag{9}$$

$$\delta_x u + \delta_y w = 0. \tag{10}$$

Equations (6) and (7) represent the linearized Navier–Stokes equations, where the density may change discontinuously at the interface positions denoted by y_s. Equation (8) is the linearized continuity equation. In equation (9) the subscript s distinguishes the value of the quantity at $y = y_s$ (the interface layer). The last equation, equation (10), expresses the incompressibility of the fluid. With perturbations of the form

$$u, w, \delta\rho, \delta p, \delta y_s \sim \exp[i(k_x x + nt)], \tag{11}$$

and assuming that the flow is aligned with the perturbation vector, i.e. $k = k_x$, we arrive at

$$\begin{aligned} &D\{\rho(n + kU)(Dw) - k\rho(DU)w\} - \rho k^2(n + kU)w \\ &\quad = iD\{\rho\nu k^2(Dw)\} - iD\{\rho\nu(D^3w)\} \\ &\qquad - D\{k\nu(\rho + \delta\rho)(D^2U)\} + i\rho\nu k^2(D^2w) - i\rho\nu k^4 w, \end{aligned} \tag{12}$$

where $D \equiv \mathrm{d}/\mathrm{d}y$. The term, $i\rho\nu k^2(D^2w)$ in equation (12) can be replaced with

$$i\rho\nu k^2(D^2w) = ik^2D[\rho\nu(Dw)] - ik^2(Dw)[D(\rho\nu)]. \tag{13}$$

The boundary condition at $y = y_s$ is determined by an integration over an infinitesimal element ($y_s - \epsilon$ to $y_s + \epsilon$), for the limit $\epsilon \rightarrow 0$. Please note that with equation (8) it follows for $\delta\rho$,

$$\delta\rho = i\frac{w}{(n + k_x U)}(D\rho). \tag{14}$$

After integration, the boundary condition becomes,

$$\begin{aligned} &\Delta_s\{\rho(n + kU)(Dw) - \rho k(DU)w\} \\ &\quad = ik^2\Delta_s\{\nu\rho(Dw)\} - i\Delta_s\{\nu\rho(D^3w)\} \\ &\qquad - k\Delta_s\{\nu\rho(D^2U)\} - ik\Delta_s\left\{\nu\frac{w}{(n + kU)}(D\rho)(D^2U)\right\} \\ &\qquad + ik^2\Delta_s\{\nu\rho(Dw)\} - ik^2\lim_{\epsilon\rightarrow 0}\int_{y_s-\epsilon}^{y_s+\epsilon}(Dw)D(\nu\rho)\,\mathrm{d}y, \end{aligned} \tag{15}$$

where Δ_s is specifying the jump of any continuous quantity f at $y = y_s$,

$$\Delta_s(f) = f_{(y=y_s+0)} - f_{(y=y_s-0)}. \tag{16}$$

For $\nu \equiv 0$, we retrieve the corresponding expression as given by Chandrasekhar (1961).

2.2 Special case: constant velocities and densities

To simplify the derivation of the growth rate n further, we consider the case of two fluid layers with constant densities ρ_1 and ρ_2, and constant flow velocities U_1 and $U_2 = -U_1$. In each region of constant $\rho_{1,2}$ and $U_{1,2}$, equation (12) reduces to

$$\begin{aligned} &\left[(n + kU_{1,2})\rho_{1,2} - 2i\nu k^2\right](D^2w) + i\nu(D^4w) \\ &\quad - k^2\left[(n + kU_{1,2}) - i\nu k^2\right]w = 0. \end{aligned} \tag{17}$$

The layers are separated at $y = y_s = 0$, and $w/(n + kU)$ must be continuous at the interface. Also, w must be finite for $y \rightarrow \infty$, so that the solution of equation (17) has the following form,

$$w = A(n + kU_1)\mathrm{e}^{+ky} \ (y < 0) \tag{18}$$

$$w = A(n + kU_2)\mathrm{e}^{-ky} \ (y > 0). \tag{19}$$

We assume that $\nu_1 = \nu_2 = \nu$ (which is the case if we consider two media with the same viscous properties). Inserting this in equation (15), the characteristic equation yields,

$$n^2 + 2\left[k(\alpha_2 U_2 + \alpha_1 U_1) - \frac{ik^2\nu}{2}\right]n \tag{20}$$

$$+ k^2\left(\alpha_2 U_2^2 + \alpha_1 U_1^2\right) - ik^3\nu\left(\alpha_2 U_2 + \alpha_1 U_1\right) = 0. \tag{21}$$

The parameters α_1, α_2 are defined by

$$\alpha_1 = \frac{\rho_1}{\rho_1 + \rho_2}, \quad \alpha_2 = \frac{\rho_2}{\rho_1 + \rho_2}. \tag{22}$$

Solving for n, we get the expression for the mode of the linear KHI:

$$\begin{aligned} n = &-\left[k(\alpha_2 U_2 + \alpha_1 U_1) - \frac{ik^2\nu}{2}\right] \\ &\pm\sqrt{-k^2\alpha_1\alpha_2(U_1 - U_2)^2 - \frac{k^4\nu^2}{4}}, \end{aligned} \tag{23}$$

applying $U_2 = -U_1 = U$ leads to

$$\begin{aligned} n = &\left[k^2U^2(\alpha_2 - \alpha_1) + \frac{ik^2\nu}{2}\right] \\ &\pm\sqrt{-4k^2\alpha_1\alpha_2U^2 - \frac{k^4\nu^2}{4}}. \end{aligned} \tag{24}$$

The mode is exponentially growing/decaying with time, if the square root of n becomes imaginary,

$$\begin{aligned} n = &\left[k^2U^2(\alpha_2 - \alpha_1)\right] \\ &+ i\left[\frac{\nu k^2}{2} \pm \sqrt{\frac{\nu^2k^4}{4} + 4k^2U^2\alpha_1\alpha_2}\right]. \end{aligned} \tag{25}$$

The first term describes oscillations (which is not of interest for the growth), the second term the growth/decay, with a damping due to the viscosity. We use this formula for the comparison with our numerical studies for different density shearing layers. For equal density shearing layers $\rho_1 = \rho_2 = \rho$, equation (25) leads to

$$n = i\left[\frac{\nu k^2}{2} \pm \left(\frac{\nu^2k^4}{4} + k^2U^2\right)^{1/2}\right]. \tag{26}$$

In Sections 4 and 5, we use the velocity in direction of the perturbation, which in the above analysis refers to the y-direction and therefore, to the v_y-velocity component (w) when comparing with simulations. The exponential term in equation (11) [$\sim\exp(i \cdot n \cdot t)$] describes the time evolution of the KHI. In the following, we therefore compare $\ln(v_y)$ with the analytical expectation $\ln(w) \sim i \cdot n \cdot t$.

Table 1. Initial conditions in dimensionless units (first column) and in cgs units (second column). In the text, we always refer to dimensionless units. The (dimensionless) KHI growth time is about $\tau_{\rm KHI} \sim 0.65$ (equal density case) and $\tau_{\rm KHI} \sim 1.12$ (density contrast of DC = 10).

Physical parameters	Dimensionless	in cgs units
Box size	2	2 cm
Mass	4	2780.81 g
Velocity	0.387	0.40 km s^{-1}
Time	1	$9.8 \cdot 10^{-6}$ s

3 KHI – NUMERICAL DESCRIPTION

We use two independent numerical approaches – particle based and grid based – to follow the hydrodynamics of the system. In the following, all physical parameters are given in code units (see Table 1 for conversion to physical units).

3.1 SPH models – VINE & P08

The parallel Tree-SPH code VINE (Nelson et al. 2009; Wetzstein et al. 2009) has been successfully applied to a number of astrophysical problems on various scales (Naab et al. 2006; Jesseit et al. 2007; Gritschneder et al. 2009a; Kotarba et al. 2009; Walch et al. 2010). In VINE, the implementation of AV is based on the description by Monaghan & Gingold (1983), and it includes the modifications by Lattanzio et al. (1986). AV is not a real physical viscosity, but implemented to allow the treatment of shock phenomena. A viscous term, Π,

$$\Pi = -\nu \left(\frac{\boldsymbol{v} \cdot \boldsymbol{r}}{r^2 + \epsilon \bar{h}^2} \right), \tag{27}$$

is added to the SPH momentum equations. The quantity $\epsilon \sim 0.01$ prevents a singularity if $r \rightarrow 0$, while $\bar{h}$ presents the mean smoothing length between two particles. For ν follows,

$$\nu = \frac{\bar{h}}{\bar{\rho}} \left(\alpha \bar{c} - \beta \frac{\bar{h} \boldsymbol{v} \cdot \boldsymbol{r}}{r^2 + \epsilon \bar{h}^2} \right), \tag{28}$$

$\bar{\rho}$, and $\bar{c}$ are the mean density and the mean sound speed, respectively. The AV parameter α controls the shear and the bulk viscosity, whereas the β parameter regulates the shock-capturing mechanism. In the following, we set $\alpha = 0.1$, and $\beta = 0.2$ if not otherwise specified. AV reduces the Reynolds number of the flow, resulting in the damping of the KHI (Monaghan 2005). Balsara (1995) proposed a corrective term, improving the behaviour of the AV in shear flows. Further improvements are discussed in Monaghan (2005) and references therein. VINE can be run with and without the 'Balsara viscosity'.

To prevent the so-called 'artificial pairing' in SPH (e.g. Schuessler & Schmitt 1981), we implement a correction developed by Thomas & Couchman (1992). Details can be found in Wetzstein et al. (2009) and Nelson et al. (2009).

The SPH code presented in P08 uses a different implementation of AV as explained in Morris & Monaghan (1997) to prevent the side effects of artificial dissipation. Additionally, a diffusion term called 'artificial thermal conductivity (ATC)' is implemented (see Section 4.2), which has been shown to prevent the KHI suppression in shear flows with large density contrasts (P08).

3.2 Grid-based models – FLASH & PLUTO

We choose the publicly available, Message Passing Interface (MPI)-parallel FLASH code version 2.5 (Fryxell et al. 2000). FLASH is based on the block-structured Adaptive Mesh Refinement (AMR) technique implemented in the PARAMESH library (MacNeice et al. 2000). However, we do not make use of the AMR refinement technique, but use uniform grids throughout this paper. In FLASH's hydrodynamic module the Navier–Stokes equations are solved using the piecewise parabolic method (Colella & Woodward 1984), which incorporates a Riemann solver to compute fluxes between individual cells. We use a Riemann tolerance value of 10^{-7} and a Courant, Friedrichs and Lewy number (CFL) of 0.5. Due to FLASH's hydrodynamic scheme, the intrinsic numerical viscosity is reduced to a minimum. This allows us to study the influence of a physical viscosity on the growth of the KHI. We therefore modify the hydrodynamical equations based on the FLASH module 'diffuse' to explicitly include a viscous term, which scales with a given kinematic viscosity (see Sections 5.1 and 5.2).

As an additional test, we apply the Godunov-type high-resolution shock capturing scheme PLUTO (Mignone et al. 2007). It is a multiphysics, multi-algorithm modular code, especially designed for the treatment of discontinuities. For the simulations described in this paper, we employ different Riemann-solvers and time-stepping methods on a uniform, static grid.

3.3 Initial conditions and analysis method

Our numerical initial conditions (ICs) are identical to the ones used for the derivation of the analytical growth rates (see Section 2, Fig. 1 and Table 1). To excite the instability, we apply a velocity perturbation in y direction:

$$v_y = v_0 \sin(k \cdot x) \cdot \exp\left[-\left(\frac{y}{\sigma_0} \right)^2 \right], \tag{29}$$

where k is the wavenumber and v_0 is the perturbation amplitude of the y-velocity triggering the instability. The parameter σ_0 controls how quickly the perturbation decreases with y (see discussion Appendix A). It is set to $\sigma_0 = 0.1$, if not otherwise specified. Initial pressure and density are set to $p_0 \equiv 1$ and $\rho_0 \equiv 1$, resulting in a sound speed of $c_{\rm s,0} = \sqrt{5/3}$ with an adiabatic exponent of $\gamma = 5/3$. Since the analysis of Section 2 is only valid for an incompressible fluid, the flow speed U must be subsonic. We chose $U \equiv 0.3 \times c_{\rm s,0} \approx 0.387$, and the initial perturbation is $v_0 = 0.1 \times U = 0.0387$. We tested the assumption of incompressibility by calculating $\nabla \cdot \boldsymbol{v}$, which vanishes for incompressible flows. This is satisfied in the linear regime, the primary focus of our work. The wavenumber k is equal to $4\ \pi/L$, where L is the box length. The simulated box ranges from $[-1, 1]$ in both directions. We use periodic boundary conditions. If not otherwise specified the AV parameters are set to $\alpha = 0.1$ and $\beta = 0.2$.

To analyse the SPH and grid simulations consistently, we bin the SPH particles on a 64^2 grid, using the cloud-in-cell method (Hockney & Eastwood 1988). For the grid codes, the same initial conditions are used. A resolution of 512^2 is adopted during the calculation, but we rebin to a 64^2 grid for the analysis.

We measure the fastest-growing mode, which is the $k = 4\pi/L$ mode of the velocity perturbation in y-direction via a Fourier analysis. For more information see Appendix B.

We perform two sets of simulations with (i) equal density layers (see Section 4.1 for SPH and Section 5.1 for grid codes) and (ii) unequal density layers (see Section 4.2 for SPH and Section 5.2 for

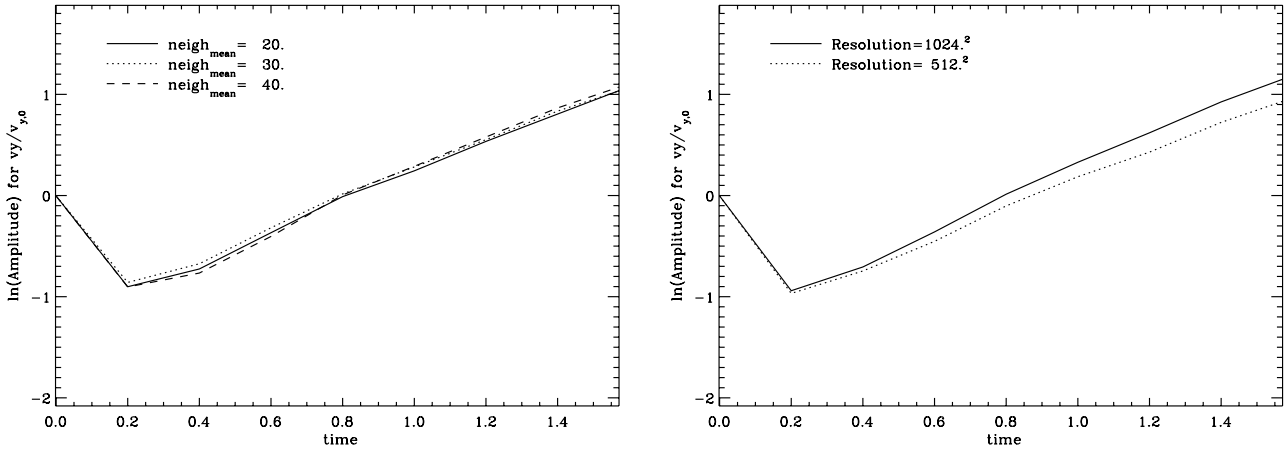

Figure 2. Time evolution of the v_y-amplitude using VINE for different numbers of mean neighbours, $\bar{n}_{\rm neigh}$, (left-hand panel) and for different particle number (right-hand panel).

grid codes). In the latter case we assume pressure equilibrium. For SPH, we investigate the effects of equal mass and different mass particles (see Section 4.2).

4 SPH SIMULATIONS OF THE KHI

In the following, we model the evolution of the KHI in systems with $\rho_1 = \rho_2$ (Section 4.1) and $\rho_1 \neq \rho_2$ (Section 4.2). We apply VINE, if not otherwise specified, and use the analytical growth rates (equations 25 and 26) derived in Section 2 to determine the effect of AV.

4.1 Fluid layers with equal densities

In the case of $\rho_1 = \rho_2$, we vary the following parameters: the resolution, which can be either enhanced by using more particles or decreasing the smoothing length h, and the AV parameters α and β. We vary one parameter at a time, while the other ones are set to the fiducial values (see Section 3.1). In the context of AV, we discuss the importance of the Balsara viscosity. In Appendix A we also discuss the influence of different σ_0, which determines the strength of the initial *vy*-perturbation (equation 29).

(i) *Dependence on resolution*

According to the smoothing procedure in the SPH scheme, each particle requires a certain number of neighbouring particles for the calculation of its physical quantities. In VINE, these range from $n_{\rm neigh,min}$ to $n_{\rm neigh,max}$. The corresponding mean value of neighbours, $\bar{n}_{\rm neigh}$, determines the smoothing length h. For a constant particle number, increasing $\bar{n}_{\rm neigh}$ leads to a larger smoothing length, while at the same time the effective resolution is decreased.

In Fig. 2, we show the time evolution of the v_y-amplitude, which describes the growth of the KHI. For $t \leq 0.2$ the amplitudes decrease since the SPH particles lose kinetic energy by moving along the y-direction into the area of the opposite stream (see Appendix A). Therefore, we only consider $t > 0.2$ when fitting the growth rates of the KHI. The left-hand panel of Fig. 2 shows the amplitude growth for $\bar{n}_{\rm neigh} = 20,\ 30$ and 40, respectively. (The commonly used value in two dimensions is $\bar{n}_{\rm neigh} = 30$.) All three cases appear to be similar. Thus, different $\bar{n}_{\rm neigh}$ do not have a substantial impact on the KHI-amplitude growth.

The right-hand panel of Fig. 2 shows the dependence on particle number, for the fiducial case of 512^2 (dotted line) and for an increased resolution of 1024^2 (solid line). The difference for the fitted viscosity is small ($\leq$1 per cent).

(ii) *Dependence of KHI on α, β*

In Figs 3, 4 and 5, we show the KHI evolution for different values of α and β without the Balsara viscosity. Increasing the AV parameter α or β results in a successive suppression of the KHI. Values of $\alpha > 2$ and $\beta > 1$ lead to a decay of the initial perturbation. However, β does not affect the growth as much as α. Therefore, we first concentrate on α as the operating term on the KHI.

Can we assign an equivalent physical viscosity $\nu_{\rm SPH}$ to the SPH scheme, i.e. can we determine how 'viscous' the fluid described by SPH is intrinsically? To quantify its value, the analytical slope (equation 26), with the viscosity being the free parameter, is fitted to the simulated growing amplitudes. We show the best fits for $\alpha = 0.125$ and 2 in the left-hand panel of Fig. 5, for which we find the intrinsic viscosity of $\nu_{\rm SPH} = 0.07$ and 0.1. Here we assumed the time range of [0.2, 1], for which we determine the fits, to be well in the linear regime.

In Fig. 6 we present the derived values of $\nu_{\rm SPH}$ as a function of α. In summary, $\nu_{\rm SPH}$ increases linearly with increasing α, and the corresponding slope is 0.039. We also derive an offset of 0.065, which is the remaining intrinsic viscosity for $\alpha = 0$. For each simulation, we also show the effective Re number of the flow (see Fig. 6, right y-axis), which was computed from $\mathrm{Re} = L \cdot U/\nu_{\rm SPH}$. The parameter L describes the characteristic scale of the perturbation, in our case the wavelength and U is the velocity of the flow. Clearly, the Reynolds numbers we reach with our models are well below the commonly expected numbers for turbulent flows ($\mathrm{Re} > 10^5$).

The effective viscosity of the flow is also influenced by different values of β. Changing β by a factor of 2 (e.g. from $\beta = 0.5$ to $\beta = 1$) results in an increase in effective viscosity by a factor of 0.01 (see right-hand panel of Fig. 5).

(iii) *Dependence on the Balsara viscosity*

We showed that AV leads to artificial viscous dissipation, resulting in the damping of the KHI. To prevent this, we use the Balsara viscosity, see also Section 3.1. In Fig. 7 we show the corresponding amplitudes for three examples of AVs: ($\alpha = 0.1, \beta = 0.2$), ($\alpha = 1, \beta = 2$) and ($\alpha = 2, \beta = 2$). Clearly, the Balsara viscosity reduces the damping of the KHI, rendering $\nu_{\rm SPH}$ almost independently of α and β (see also Fig. 6).

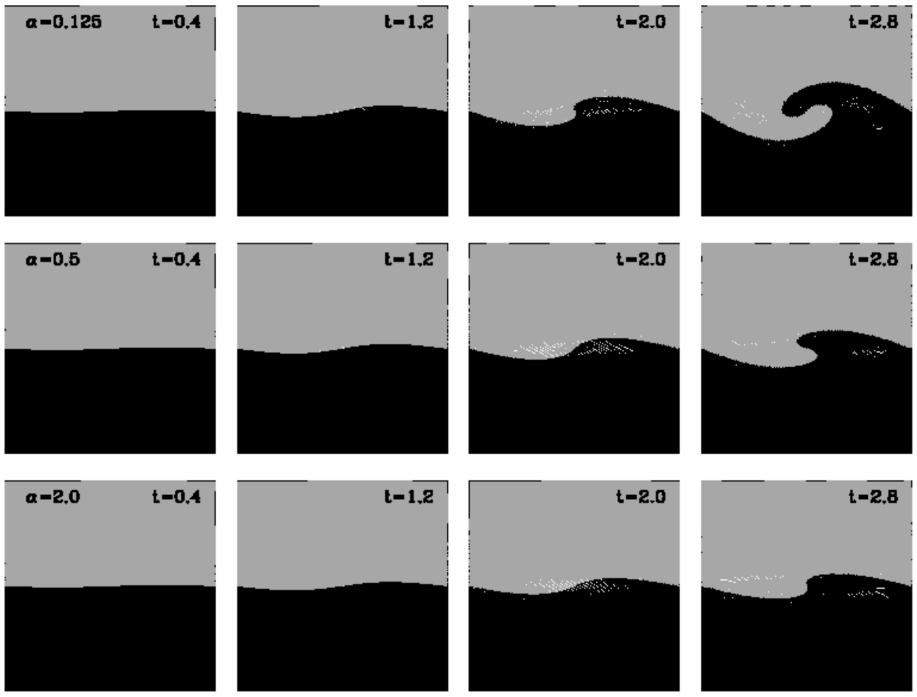

Figure 3. Time evolution of the KHI using VINE for increasing AV parameter α (top to bottom) and constant $\beta = 2$. The panels show the central region of each simulation box, ranging $[-0.5, 0.5]$. The upper layer (grey area) is moving to the left, the lower layer (black area) to the right. Noticeable damping occurs for $\alpha > 0.125$ (see left-hand panel of Fig. 5).

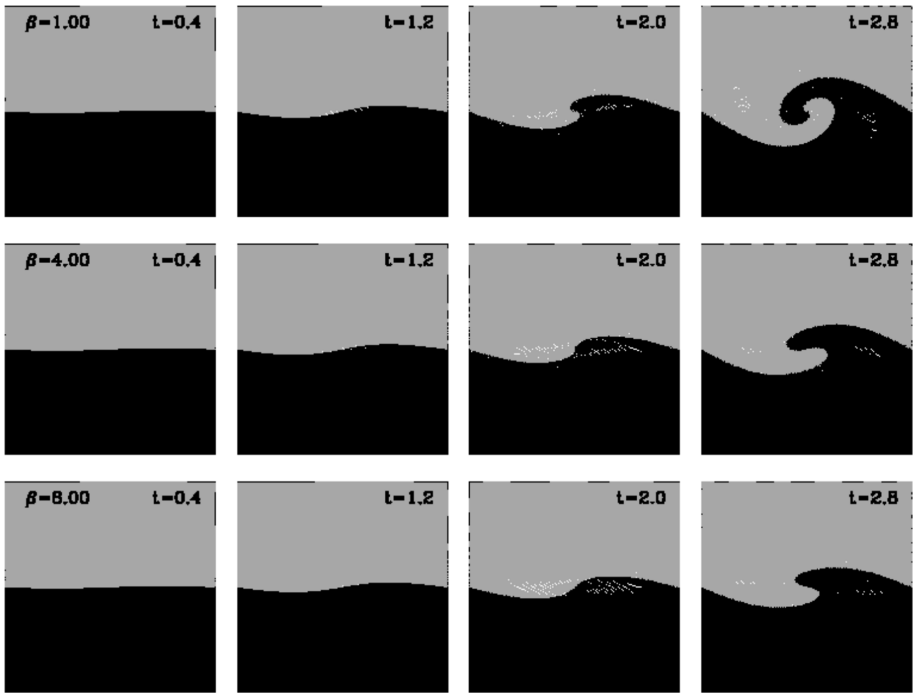

Figure 4. Like Fig. 3 but for increasing values of the AV parameter β ($\alpha = 0.1$). A noticeable damping occurs for of $\beta > 1$ (see right-hand panel of Fig. 5).

4.2 Fluid layers with variable densities

While the previously addressed case of equal densities helped us to understand the detailed evolution of the KHI as modelled with SPH, the astrophysically more interesting case are shear flows with different densities. The resolution of the diffuse region is lower by a factor of $\sqrt{\mathrm{DC}}$, where DC is the ratio of the densities in dense and diffuse medium (e.g. DC = 10 corresponds to a density contrast of 10 : 1). We return to our standard set of parameters, in which case $\alpha = 0.1$ and $\beta = 0.2$. For these low AV parameters we do not need the Balsara viscosity (see Section 4.1). (None the less, we did run test simulations with the Balsara switch, which we found to confirm

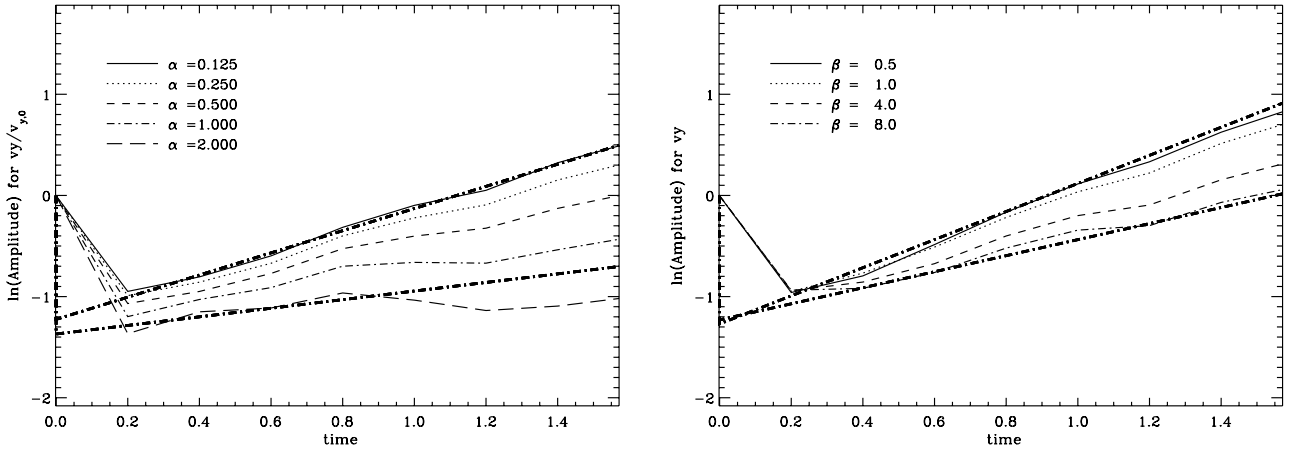

Figure 5. Left-hand panel: time evolution of the VINE v_y-amplitude for different values of the AV parameter α, where β has been fixed to $\beta = 2$. The thick dot–dashed lines correspond to the analytical fit, shown for $\alpha = 0.125$ and 2 (which correspond to $\nu_{\rm SPH} = 0.07$ and 0.1). Right-hand panel: like before, but for different values of the AV parameter β, where α has been fixed to $\alpha = 0.1$.

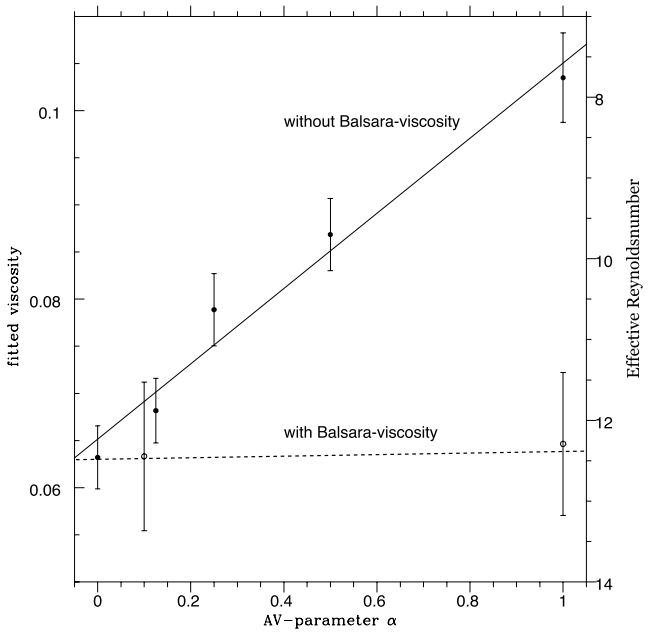

Figure 6. Derived physical viscosities ($\nu_{\rm SPH}$) corresponding to different AV parameters α with (open points) and without (filled black points) Balsara viscosity. We also show the corresponding effective *Re* numbers.

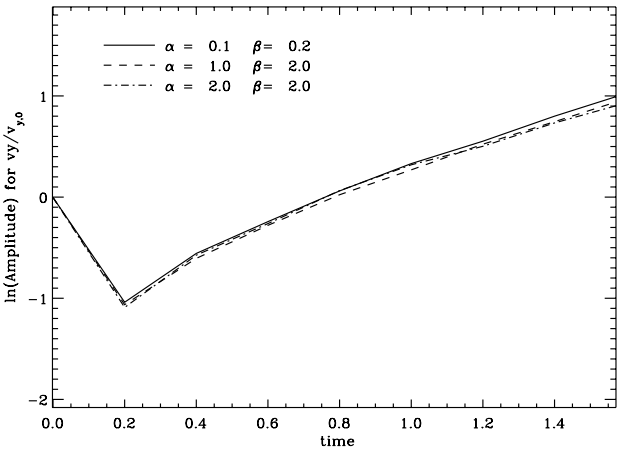

Figure 7. Time evolution of the VINE v_y-amplitude for different values of the AV parameters α and β, where the Balsara viscosity has been used. The damping of the amplitudes is completely prohibited by the Balsara switch.

our former finding, since the growth of the KHI was not affected.) In the following, we (i) analyse the growth of the KHI for different values of DC (with equal mass particles) and address the problem of KHI suppression, while in (ii) we test the influence of equal mass or spatial resolution.

(i) *KHI growth as a function of* DC

We show the KHI evolution for increasing DC in Fig. 8. For DC $\geq$ 6, the KHI does not develop anymore. This SPH problem of KHI suppression has been studied in great detail (e.g. Agertz et al. 2007; P08; Wadsley et al. 2008; Abel 2010; Read et al. 2010). SPH particles located at the interface have neighbours at both sides of the boundary (i.e. from the dense and less dense region). Therefore, the density at the boundary is smoothed during the evolution. However, the corresponding entropy (or, depending on the specific code, the thermal energy) is artificially fixed in these (isothermal) setups which results in an artificial contribution to the SPH pressure force term, due to which the two layers are driven apart. One possible solution is to either adjust the density (Ritchie & Thomas 2001; Read et al. 2010), or to smooth the entropy (thermal energy) (P08; Wadsley et al. 2008; Abel 2010).

A remedy has been discussed by P08, who proposed to add a diffusion term, which is called ATC, to adjust the thermal energy. (For a detailed study of ATC see P08.) With this method, the KHI should develop according to the test cases of P08.

In Fig. 9, we test whether the P08 approach is indeed in agreement with our analytical prediction. Note that P08 has a method implemented to account for the artificial viscous dissipation caused by AV (similar to the Balsara viscosity). Thus, the viscous effects of AV are strongly reduced. For DC = 10 and using 512^2 particles in the dense layer, we indeed find good agreement between measured and analytical growth rates. If the standard SPH scheme is used, a correction term like ATC has to be included to obtain a KHI in shear flows with different densities, which is consistent with the analytical prediction.

(ii) *KHI growth using equal and different particle masses*

First, we investigate the development of the KHI for the standard SPH case of equal mass resolution throughout the computational

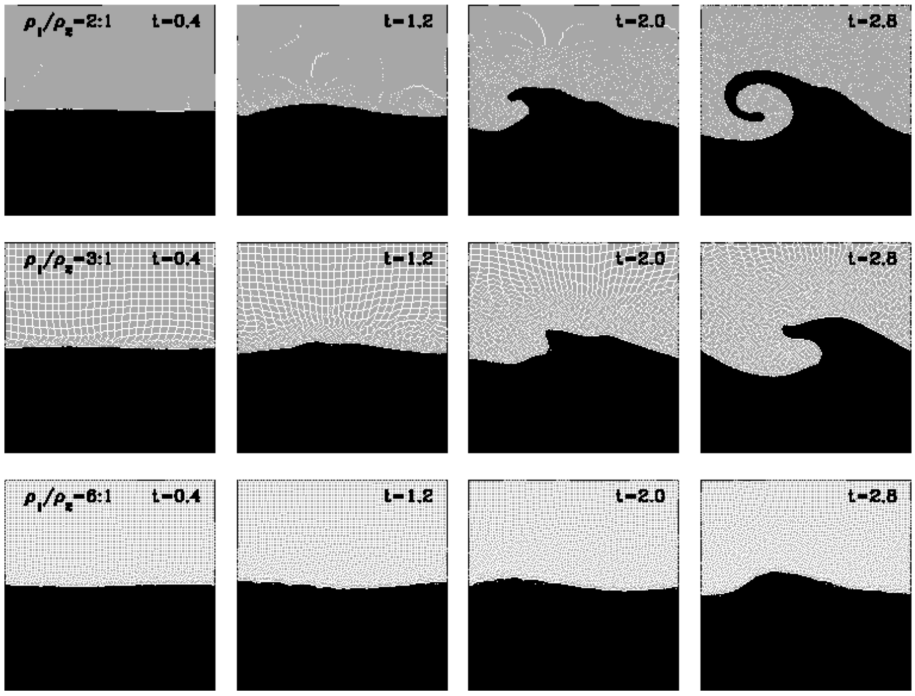

Figure 8. Like Fig. 10 top panel, but for different density contrasts. From top to bottom, we show DC = 2, 3, 6. For DC ≥ 6 the KHI does not develop anymore.

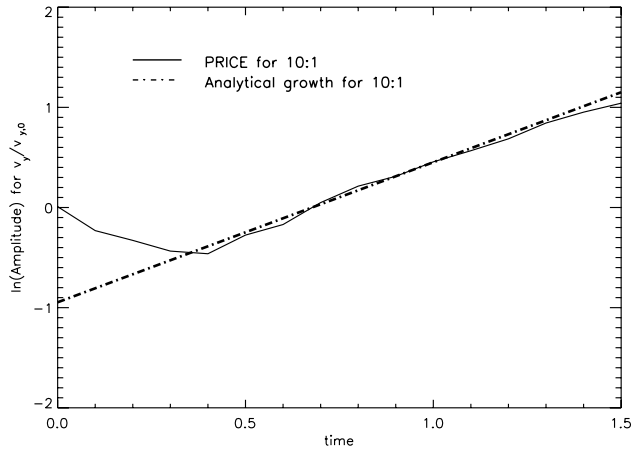

Figure 9. Time evolution of the KHI modelled with P08 for the DC = 10. The dot–dashed line corresponds to the analytical prediction, equation (30), which is in good agreement with the simulation.

domain, and therefore fewer particles in the low-density fluid layer (see top panel of Fig. 10 for DC = 10, where the dense medium is resolved with 512^2 particles). This results in a varying spatial resolution, due to the fact that SPH derives the hydrodynamic quantities within a smoothing length h set by a fixed number of nearest neighbours. This construct – as has been discussed in detail earlier in e.g. Agertz et al. (2007) – specifically lowers the Reynolds number of the shear flow across density discontinuities, thus affecting the evolution of the KHI. As can be seen in the top panel of Fig. 10, the KHI is completely suppressed.

Secondly, we test the case of equal spatial resolution in both fluid layers, and therefore unequal particle masses within the computational domain (Fig. 10, lower panel). Again, we find the KHI to grow too slowly with respect to the analytical estimate. However, the suppression is less effective in the latter case.

5 GRID SIMULATIONS OF THE KHI

For comparison to the SPH treatment of KHI, we study an identical setup of fluid layers with the grid-based codes FLASH and PLUTO (see Section 3.2). We reuse the previously specified initial conditions with a grid resolution of 512^2 cells in the standard case. For FLASH, we additionally include physical viscosity of various strength in some of the simulations (see Section 3.2). Note, that for the following examples we use $\sigma_0 = 1$ if not otherwise specified, which does not affect the growth of the amplitudes in the linear regime (for further information see discussion in the Appendix A).

5.1 Fluid layers with equal densities

5.1.1 Non-viscous evolution

The left-hand panel of Fig. 11 shows the non-viscous KHI evolution, using FLASH (solid line), PLUTO (dotted line) and for comparison VINE (dashed line). In the VINE example, the AV has been set to zero ($\alpha = \beta = 0$). The expected analytical growth (equation 26) reduces with $\nu = 0$ to $n \sim k \cdot U = 2.43$ (indicated by the thick dot–dashed line). The FLASH and PLUTO amplitudes develop in a similar pattern and are almost undistinguishable. Their fitted slopes within the linear regime (which lies roughly between $t = 0.3$ and 0.6) results in $n_{\rm fit} = 2.49$. FLASH and PLUTO show a consistent growth in agreement with the analytical prediction. VINE on the other hand exhibits a slightly slower growth. This deviation is due to the intrinsic viscosity ($\nu_{\rm int} = 0.065$) that was estimated in 4.1.

5.1.2 Viscous evolution

The right-hand panel of Fig. 11 shows the viscous KHI amplitudes using FLASH. The corresponding analytical predictions (equation 26) are shown by the thick dot–dashed lines for the examples with $\nu = 0.00003$ and $\nu = 0.03$. To quantify the growth of the KHI in the FLASH simulations, we again fit the slopes of the KHI amplitude in

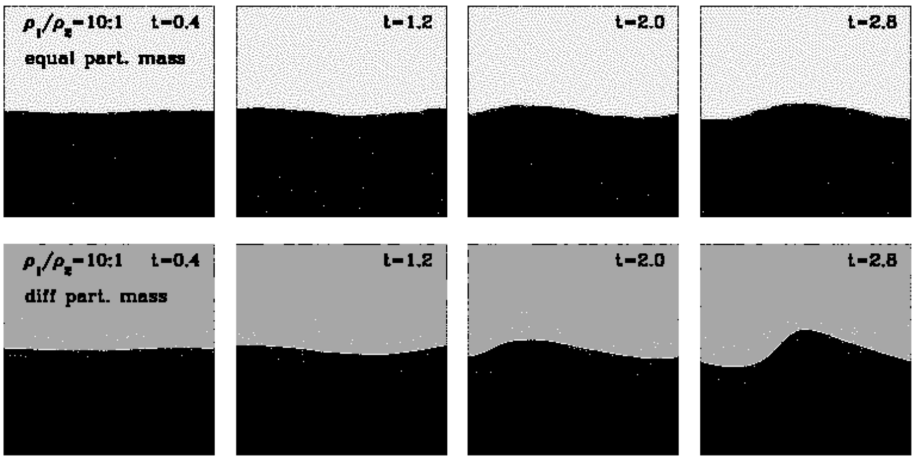

Figure 10. KHI with VINE for DC = 10. Top: case of equal particle masses. Bottom: case of unequal particle masses and therefore equal particle numbers in both layers. The KHI is suppressed in all cases.

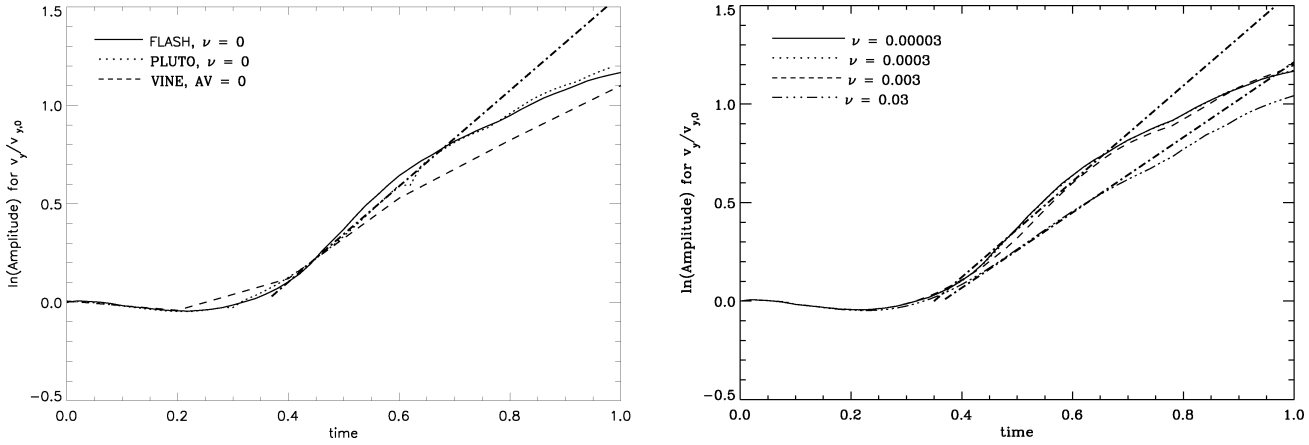

Figure 11. Evolution of KHI amplitudes for equal density layers. Left-hand panel: non-viscous evolution for FLASH (solid line) and PLUTO (dotted line). Additionally, we show the example with VINE (dashed line), where the AV has been set to zero ($\alpha = \beta = 0$). Right-hand panel: viscous KHI evolution using FLASH. The thick dot-dashed lines correspond to the analytical prediction, equation (26).

the linear regime (between $t = 0.3$ and 0.6). The result along with the corresponding error is plotted in Fig. 12. For small viscosities ($\nu < 0.003$), we find the growth rates of the KHI in FLASH to be in good agreement with the analytical prediction. In this viscosity range, the dominant term in the analytical prediction (equation 26) is $\sim kU$. Therefore, any influence of ν is marginal, and the amplitudes do not change considerably. FLASH treats the fluid as if $\nu \approx 0$.

However, with increasing viscosity, the amplitudes should be damped. This behaviour is in fact visible in the right-hand panel of Fig. 11 (as well as in Fig. 12). The growth rates of the KHI agree very well with the analytical prediction.

5.2 Fluid layers with different densities

5.2.1 Non-viscous evolution

Finally, we investigate a density contrast of 10 : 1, similar to the example studied with VINE (see Section 4.2). Fig. 13 shows the non-viscous evolution of the KHI for the DC = 10 case (upper line for FLASH, bottom line for PLUTO). It can be seen that for both codes the interface layer starts to roll-up and the instability is developed. This is in disagreement with the previously discussed case using SPH, where the KHI is completely suppressed for DC > 6 (see 4.2).

The left-hand panel of Fig. 14 presents the corresponding amplitudes for FLASH (solid line) and PLUTO (dotted line) compared to the analytical prediction (thick dot–dashed line), which in this case reduces to

$$n = \pm i\sqrt{4k^2U^2\alpha_1\alpha_2}. \tag{30}$$

For FLASH we show two different resolutions (512^2 and 1024^2). The amplitudes resulting in the case of low and high resolution are effectively indistinguishable. This is an important result, as it demonstrates that small-scale perturbations, which arises due to numerical noise and which could violate the linear analysis (as we then might follow the growth of higher order modes rather than the initial perturbation) are not important. Therefore, we have shown that our simulations are converged as we would otherwise expect the growth of the KHI to be slightly dependent on the grid resolution (see e.g. the recent findings of Robertson et al. 2010, who had to smooth the density gradient between the two fluid layers in order to achieve convergence in terms of grid resolution). Moreover, both FLASH and PLUTO evolve similarly. For all three examples the slope of the amplitude evolution can be approximated to 1.4, which is in good agreement with the analytical expectation. Note that we do not show the comparison with the VINE amplitude since the KHI does not evolve for DC = 10 (see Section 4.2).

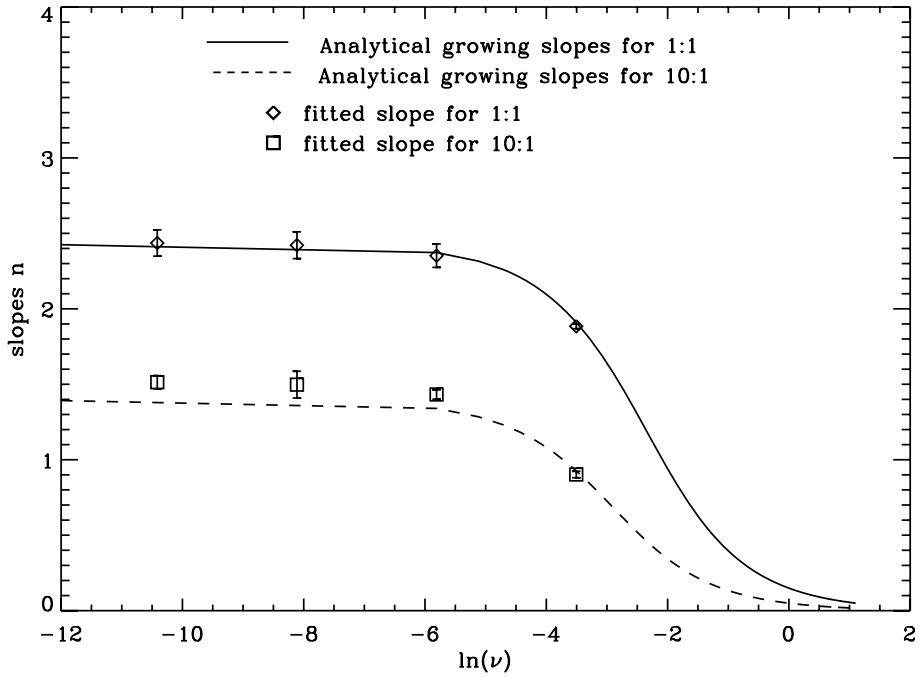

Figure 12. Comparison of the analytical expectation and the models for DC = 1 (diamond shaped symbols) and DC = 10 (square symbols). The slopes derived for FLASH correspond to the analytical fits. The lines represent the analytic prediction, for DC = 1 (solid line, see equation 26) and DC = 10 (dashed line, see equation 25).

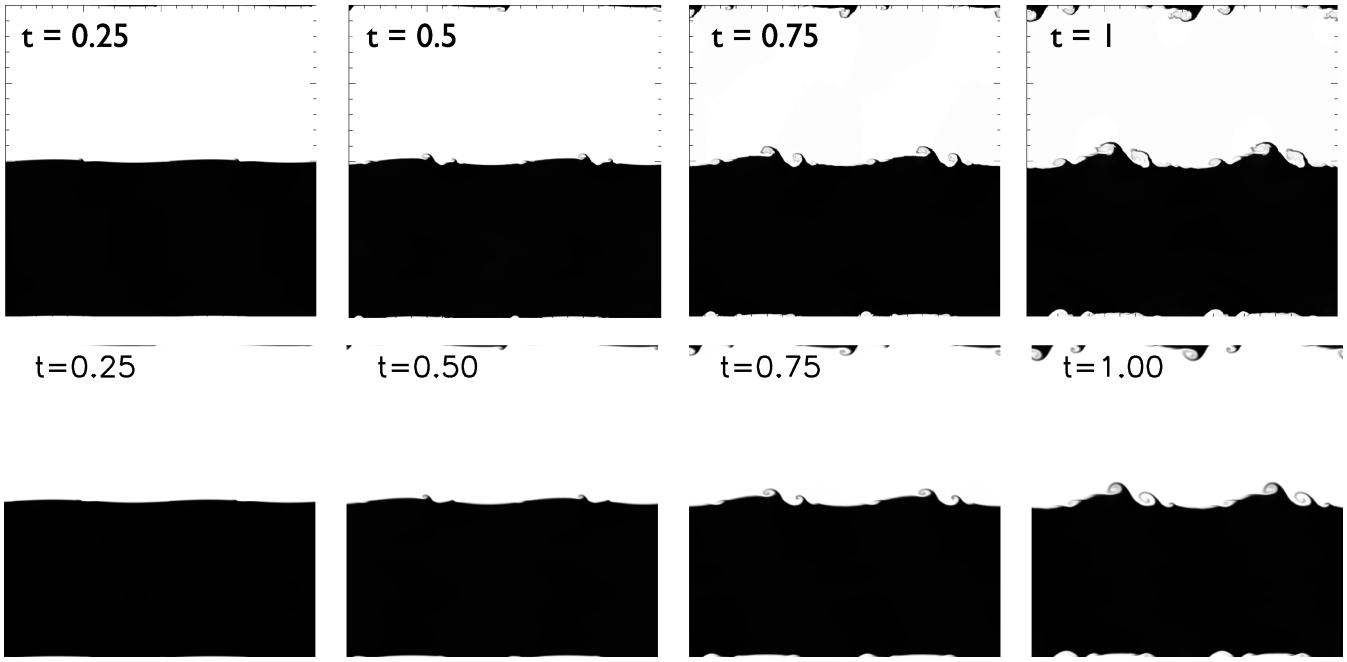

Figure 13. Time evolution of the KHI density in a simulation with $\nu = 0$ and DC = 10 for FLASH (top row) and PLUTO (bottom row). The plotted box size is from $[-1, 1]$ in both directions, the resolution is 512^2. The KHI develops, which is in contrast to the example simulated with VINE.

Many grid codes offer a variety of hydrodynamical solvers. We therefore tested the influence of different numerical schemes on the growth of the KHI using PLUTO (see right-hand panel of Fig. 14). We show three different examples: 'sim000' is a Lax–Friedrichs scheme together with a second-order Runge–Kutta solver (tvdlf); 'sim001' implements a two-shock Riemann solver with linear reconstruction embedded in a second-order Runge–Kutta scheme; 'sim002' also implements a two-shock Riemann solver, but with parabolic reconstruction, and embedded in a third-order Runge–Kutta scheme. Both, 'sim001' and 'sim002' show a similar growth of the KHI in agreement with the analytical prediction (see Fig. 14, top-right panel). The more diffusive scheme used in 'sim000' causes a small delay in the growth of the KHI, but results in a similar slope within the linear regime (up to $t = 0.6$).

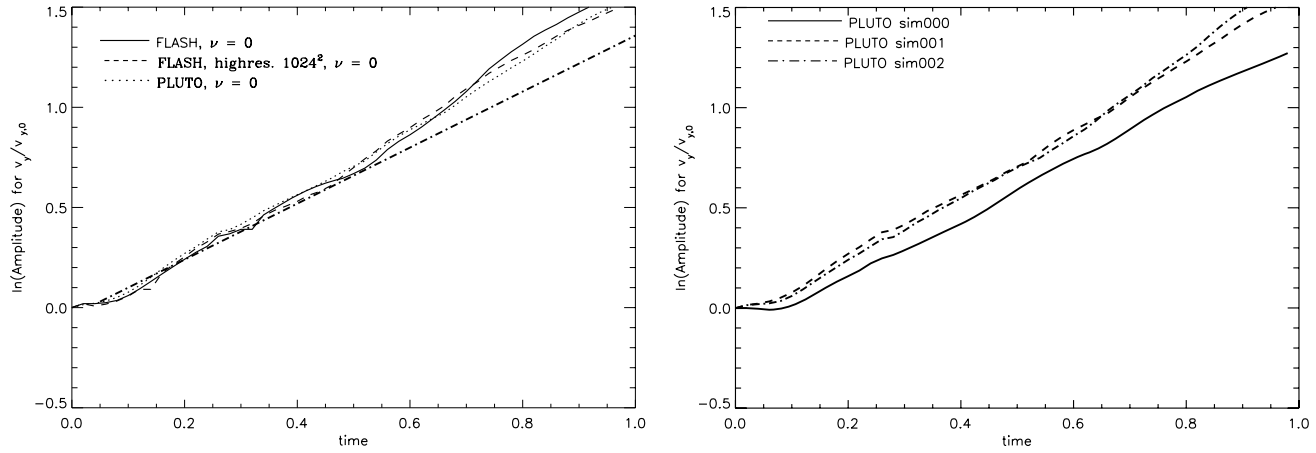

Figure 14. The same as in Fig. 11 but for a DC = 10. Left-hand panel: non-viscous evolution for FLASH (solid line), PLUTO (dotted line) and the high-resolution (1024^2) amplitude for FLASH (dashed line). Right-hand panel: non-viscous evolution using PLUTO, with different solvers, see text for more details.

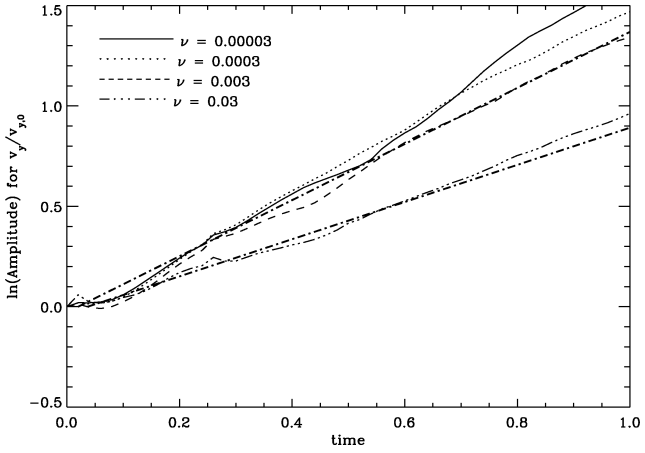

Figure 15. Viscous evolution using FLASH. The thick dot–dashed lines correspond to the analytical prediction, equation (25).

5.2.2 Viscous evolution

Fig. 15 shows the viscous KHI amplitudes using FLASH, which are increasingly suppressed with ν. The corresponding analytical prediction (equation 25) is shown for $\nu = 0.0003$ and 0.03 (thick dot–dashed lines). For $\nu < 0.03$, the simulated growth rate is slightly enhanced by a factor of $\sim$0.12 as compared to the analytical prediction (see also Fig. 12). However, for higher viscosities ($\nu \geq 0.03$) we find good agreement between simulation and analytical prediction.

6 CONCLUSIONS

We have studied the KHI applying different numerical schemes. We use two methods for our SPH models, namely the Tree-SPH code VINE (Nelson et al. 2009; Wetzstein et al. 2009), and the code developed by P08. The grid-based simulations of the KHI rely on FLASH (Fryxell et al. 2000), while as a test for the non-viscous evolution we also apply PLUTO (Mignone et al. 2007).

We first extended the analytical prescription of the KHI by Chandrasekhar (1961) to include a constant viscosity. With this improvement we were able to measure the intrinsic viscosity of our subsequently performed numerical simulations. We test both SPH as well as grid codes with this method.

We then concentrated on the KHI evolution with SPH. We performed a resolution study to measure the dependence of the KHI growth on the mean number of SPH neighbours ($\bar{n}_{\rm SPH}$) and the total number of particles, respectively. We found that our simulations were well resolved and that a different number of $\bar{n}_{\rm SPH}$ did not significantly influence the KHI growth rate.

In case of equal density shearing layers, we then measured the intrinsic viscosity in VINE by evaluating our simulations against the analytical prediction in the linear regime. Without using the Balsara viscosity the AV parameters α and β effectively lead to a damping of the KHI. The commonly suggested and used settings of $\alpha = 1$ and $\beta = 2$ result in a strong suppression of the KHI. More quantitatively, we derive values of $0.065 < \nu_{\rm SPH} < 0.1$ for $0 < \alpha < 1$. Different values of β do not have a strong impact on $\nu_{\rm SPH}$. By introducing the Balsara viscosity the dissipative effects of the AV can be reduced significantly, effectively rendering the results to be independent of α and β. However, the constant floor viscosity of $\nu_{\rm SPH} = 0.065$ prevails. Furthermore for a given α, we estimated the effective Reynolds number (Re) of the flow. For the minimum SPH viscosity of $\nu_{\rm SPH} = 0.065$ we derive a maximum Reynolds number of 12. This is very small compared to typical Reynolds numbers of real turbulent flows ($\mathrm{Re} > 10^5$). For different density shearing layers, we confirmed the results discussed in Agertz et al. (2007), i.e. the KHI is completely suppressed for shear flows with different densities (in the case of VINE for DC $\geq$ 6). Here, using the Balsara switch does not solve the problem. This indicates that other changes to the SPH formalism are required in order to correctly model shearing layers of different densities. To demonstrate this we applied the solution of P08 to our initial conditions for DC = 10. In this case the KHI was suppressed in VINE. However, we found good agreement between the analytically predicted amplitude evolution and the simulation of P08 for DC = 10.

The second part of this paper addresses the non-viscous and viscous KHI evolution using grid codes. In the case of equal density shearing layers, we found the non-viscous growth rates for shear flows with FLASH and PLUTO to be in good agreement with the analytical prediction. In the viscous case, the FLASH amplitudes show only a minor dependency on the viscosity if $\nu < 0.03$. Increasing the viscosity leads to a damped evolution, with the simulated growth coinciding with the analytical prediction.

For non-viscous shear flows (with a density contrast of DC = 10), the KHI does develop for FLASH and PLUTO in agreement with

the analytical prediction. In the viscous case FLASH (also analysed with DC = 10) slightly overpredicts the corresponding growth rates for $\nu < 0.03$ by a constant factor of $\sim$0.12.

The comparison between VINE, FLASH and PLUTO in the equal density case, where $AV = 0$ and $\nu = 0$, demonstrated that VINE does have an intrinsic viscosity (which we estimated to $\nu_{\rm int} \sim 0.065$).

ACKNOWLEDGMENTS

We would like to thank Volker Springel for his useful suggestions, Thorsten Naab for his support, Oscar Agertz for helpful discussions, as well as Eva Ntormousi. Many thanks also to the referee. This research was supported by the DFG priority programme SPP 1177 and by the DFG cluster of excellence 'Origin and Structure of the Universe'. Part of the simulations were run on the local SGI ALTIX 3700 Bx2 which was also partly funded by this cluster of excellence. FLASH was developed by the DOE-supported ASC/Alliance Center for Astrophysical Thermonuclear flashes at the University of Chicago. SW gratefully acknowledges the support of the EC-funded Marie Curie Research Training Network CONSTELLATION (MRTN-CT-2006-035890). MW gratefully acknowledges support from NSF grant 0707731.

REFERENCES

Abel T., 2010, preprint (arXiv:1003.0937)
Agertz O. et al., 2007, MNRAS, 380, 963
Agertz O., Teyssier R., Moore B., 2009, MNRAS, 397, L64
Balsara D. S., 1995, J. Comput. Phys., 121, 357
Banerjee R., Klessen R. S., Fendt C., 2007, ApJ, 668, 1028
Benz W., 1990, in Buchler J. R., ed., NATO Sci. Ser. C, Numerical Modelling of Nonlinear Stellar Pulsations: Problems and Prospects. Kluwer, Dordrecht, p. 269
Bland-Hawthorn J., Sutherland R., Agertz O., Moore B., 2007, ApJ, 670, L109
Burkert A., 2006, Comptes Rendus Physique, 7, 433
Burkert A., Naab T., Johansson P. H., Jesseit R., 2008, ApJ, 685, 897
Carroll J. J., Frank A., Blackman E. G., Cunningham A. J., Quillen A. C., 2009, ApJ, 695, 1376
Cartwright A., Stamatellos D., 2010, preprint (arXiv:1004.3694)
Chandrasekhar S., 1961, Hydrodynamic and Hydromagnetic Stability. Dover Press, New York
Colagrossi A., 2004, PhD thesis, Univ. Roma
Colella P., Woodward P. R., 1984, J. Comput. Phys., 54, 174
Couchman H. M. P., Thomas P. A., Pearce F. R., 1995, ApJ, 452, 797
Das S., Chattopadhyay I., 2008, New Astron., 13, 549
Dekel A. et al., 2009, Nat, 457, 451
Diemand J., Kuhlen M., Madau P., Zemp M., Moore B., Potter D., Stadel J., 2008, Nat, 454, 735
Español P., Revenga M., 2003, Phys. Rev. E, 67, 026705
Evrard A. E., Summers F. J., Davis M., 1994, ApJ, 422, 11
Flebbe O., Muenzel S., Herold H., Riffert H., Ruder H., 1994, ApJ, 431, 754
Fryxell B. et al., 2000, ApJS, 131, 273
Funada T., Joseph D. D., 2001, J. Fluid Mech., 445, 263
Gingold R. A., Monaghan J. J., 1977, MNRAS, 181, 375
Grcevich J., Heitsch F., Putman M., 2010, BAAS, 42, 480
Gritschneder M., Naab T., Burkert A., Walch S., Heitsch F., Wetzstein M., 2009a, MNRAS, 393, 21
Gritschneder M., Naab T., Walch S., Burkert A., Heitsch F., 2009b, ApJ, 694, L26
Heinzeller D., Duschl W. J., Mineshige S., 2009, MNRAS, 397, 890
Heitsch F., Putman M. E., 2009, ApJ, 698, 1485
Hernquist L., Katz N., 1989, ApJS, 70, 419
Hockney R. W., Eastwood J. W., 1988, Computer simulation using particles. Hilger, Bristol
Jesseit R., Naab T., Peletier R. F., Burkert A., 2007, MNRAS, 376, 997
Kaiser C. R., Pavlovski G., Pope E. C. D., Fangohr H., 2005, MNRAS, 359, 493
Katz N., Hernquist L., Weinberg D. H., 1992, ApJ, 399, L109
Kotarba H., Lesch H., Dolag K., Naab T., Johansson P. H., Stasyszyn F. A., 2009, MNRAS, 397, 733
Lanzafame G., Belvedere G., Molteni D., 2006, A&A, 453, 1027
Lattanzio J., Monaghan J., Pongracic H., Schwartz M., 1986, SIAM J. Sci. Statistical Comput., 7, 591
Lucy L. B., 1977, AJ, 82, 1013
MacNeice P., Olson K. M., Mobarry C., de Fainchtein R., Packer C., 2000, Comput. Phys. Communications, 126, 330
Marri S., White S. D. M., 2003, MNRAS, 345, 561
Mignone A., Bodo G., Massaglia S., Matsakos T., Tesileanu O., Zanni C., Ferrari A., 2007, ApJS, 170, 228
Monaghan J. J., 1992, ARA&A, 30, 543
Monaghan J. J., 2005, Rep. Progress Phys., 68, 1703
Monaghan J. J., Gingold R. A., 1983, J. Comput. Phys., 52, 374
Morris J. P., Monaghan J. J., 1997, J. Comput. Phys., 136, 41
Murray S. D., White S. D. M., Blondin J. M., Lin D. N. C., 1993, ApJ, 407, 588
Naab T., Jesseit R., Burkert A., 2006, MNRAS, 372, 839
Navarro J. F., Frenk C. S., White S. D. M., 1995, MNRAS, 275, 56
Nelson A. F., Wetzstein M., Naab T., 2009, ApJS, 184, 326
Park M., 2009, ApJ, 706, 637
Price D. J., 2008, J. Comput. Phys., 227, 10040 (P08)
Quilis V., Moore B., 2001, ApJ, 555, L95
Read J. I., Hayfield T., Agertz O., 2010, MNRAS, 405, 1513
Ritchie B. W., Thomas P. A., 2001, MNRAS, 323, 743
Robertson B. E., Kravtsov A. V., Gnedin N. Y., Abel T., Rudd D. H., 2010, MNRAS, 401, 2463
Schuessler I., Schmitt D., 1981, A&A, 97, 373
Serna A., Domínguez-Tenreiro R., Sáiz A., 2003, ApJ, 597, 878
Sijacki D., Springel V., 2006, MNRAS, 371, 1025
Springel V., 2010, MNRAS, 401, 791
Springel V., Hernquist L., 2002, MNRAS, 333, 649
Steinmetz M., Navarro J. F., 1999, ApJ, 513, 555
Steinmetz M., Navarro J. F., 2002, New Astron., 7, 155
Takeda H., Miyama S. M., Sekiya M., 1994, Progress Theor. Phys., 92, 939
Thacker R. J., Couchman H. M. P., 2000, ApJ, 545, 728
Thacker R. J., Tittley E. R., Pearce F. R., Couchman H. M. P., Thomas P. A., 2000, MNRAS, 319, 619
Thomas P. A., Couchman H. M. P., 1992, MNRAS, 257, 11
Vietri M., Ferrara A., Miniati F., 1997, ApJ, 483, 262
Wadsley J. W., Veeravalli G., Couchman H. M. P., 2008, MNRAS, 387, 427
Walch S., Naab T., Whitworth A., Burkert A., Gritschneder M., 2010, MNRAS, 402, 2253
Wetzstein M., Nelson A. F., Naab T., Burkert A., 2009, ApJS, 184, 298

APPENDIX A: DEPENDENCE OF KHI AMPLITUDES ON σ_0

Dependence of KHI on σ_0

This parameter determines the strength of the initial v_y-perturbation (equation 29). In Fig. 2 we show the time evolution of the vy-amplitude, which describes the growth of the KHI. For $t \leq 0.2$ the amplitudes decrease since the SPH particles lose kinetic energy by moving along the y-direction into the area of the opposite stream. If the magnitude of the initial perturbation is low (i.e. small σ_0), then the decrease in the amplitude is stronger than for e.g. $\sigma_0 = 1$, where the initial perturbation is large and the decrease less prominent. But independently of the value of σ_0, the subsequent growth of the instability is similar, and we obtain comparable results neglecting the decreasing initial part. Fig. A1 shows the dependency of the KHI amplitudes using different values of σ_0, for

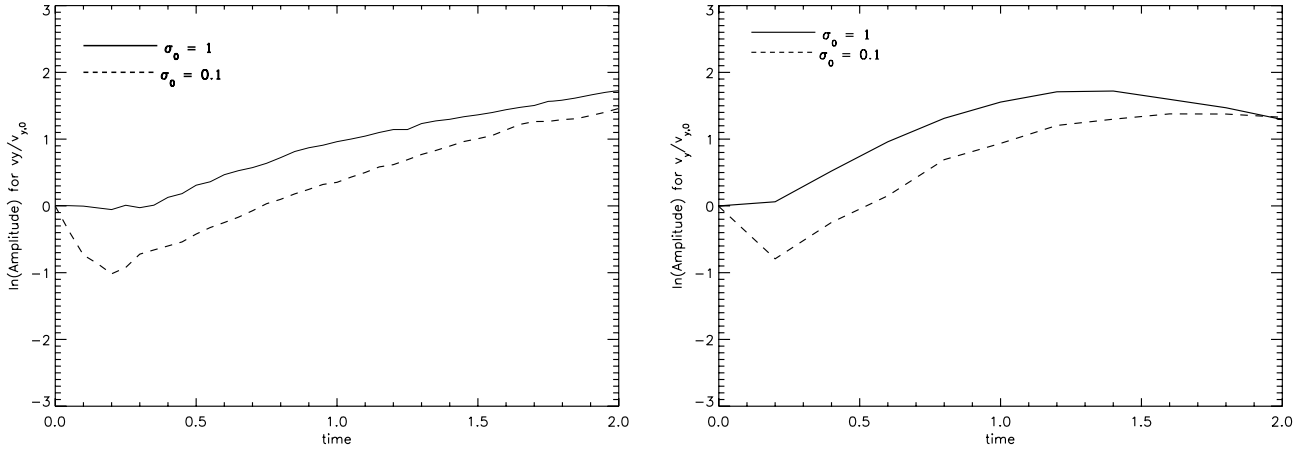

Figure A1. Variation of KHI amplitude in the case of equal density layers using VINE (left-hand side) and FLASH (right-hand side) for different values of σ_0. For FLASH the viscosity has been set to $\nu = 0.3$.

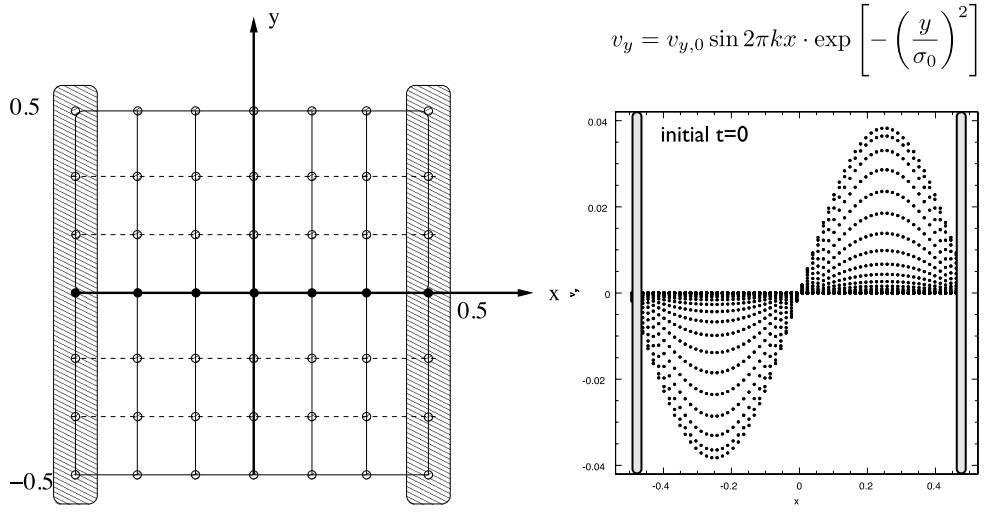

Figure B1. Method to measure the KHI amplitudes. The v_y-velocity of the particles within the shaded region are subject to the Fourier transformation. The maximum of the Back transformation gives the maximal amplitude.

VINE (left-hand side) and FLASH (right-hand side). For this example we use equal density layers, where for FLASH a viscosity of $\nu = 0.3$ has been taken. Clearly visible is the initial drop caused by a low value of σ_0. This is the case for both codes, and arises due to the transformation of energy to build up the KHI. The fitted slopes do not vary much with σ_0. To extract the slopes, we concentrate on the time evolution after this initial drop.

APPENDIX B: MEASURING THE KHI AMPLITUDES

To measure the amplitude growth of the KHI, we apply a Fourier transformation (FT) to the v_y-velocity component of the grid points. The FT allows to select the desired modes reducing the numerical noise.

The region of our focus, $x = [-0.5, 0.5]$ and $y = [\,-0.5, 0.5]$ contains one mode of the v_y-perturbation (equation 29) triggering the instability, see Fig. B1. The shaded regions comprise the particles subject to the FT (at $x = -0.5$ and 0.5). The maximum of the FT gives the dominant mode k and its corresponding velocity amplitude, which we compare with the analytical model.

This paper has been typeset from a TEX/LATEX file prepared by the author.